Modeling of the SCR reactor for coal-fired power plants: Impact of NH_3 inhibition on Hg^0 oxidation

Alessandra Beretta [a,*], Nicola Usberti [a], Luca Lietti [a], Pio Forzatti [a], Miriam Di Blasi [b], Andrea Morandi [b], Cristiana La Marca [b]

[a] *Laboratory of Catalysis and Catalytic Processes, Dipartimento di Energia, Politecnico di Milano, Piazza Leonardo da Vinci 32, 20133 Milano, Italy*
[b] *ENEL Ingegneria e Ricerca SpA, via A. Pisano 120, 56122 Pisa, Italy*

Received 18 April 2014
Received in revised form 27 June 2014 Accepted 28 June 2014
Available online 17 July 2014

1. Introduction

Among the various air pollutants emitted from coal-fired power plants, elemental mercury is a major environmental issue that has attracted considerable attention in recent year [1–4]. A variety of solutions have been studied to develop efficient and cost-effective technologies to remove mercury from coal-fired power plants, including conventional air pollution control devices (APCDs), sorbent injection, electro-catalytic oxidation, photochemical oxidation, injection of oxidizing agents and catalytic oxidation [5]; a very comprehensive review of patents and papers on the several technical solutions proposed for mercury abatement has been recently given by Gao et al. [1].

Mercury (with typical concentrations of 10–100 $\mu g/m^3$) exists in three forms in coal-fired flue gas: elemental mercury (Hg^0), oxidized mercury (Hg^{2+}, mostly in the form of $HgCl_2$), and particle-bound mercury (Hg(p)) [6–8]. Hg^{2+} and Hg(p) are relatively easy to remove from flue gas by using typical APCDs, such as ESPs and wet-FGD. Elemental mercury, Hg^0, instead, is difficult to capture

* Corresponding author. Tel.: +39 0223993284; fax: +39 0223993318.
E-mail address: alessandra.beretta@polimi.it (A. Beretta).

Notation

α	NH_3/NO inlet ratio
A_{Sup}	Surface area [m^2/g]
AV	Area velocity = volumetric flow rate/monolith geometric surface [Nm/h]
C_i	Concentration of i-th species [mol/cm^3]
Γ_{NO,NH_3}	NO, NH_3 dimensionless concentration = C_i/C^0_{Hg}
Γ_{Hg}	Hg^0 dimensionless concentration = C_{Hg}/C^0_{Hg}
ΔH_{NH_3}	Heat of adsorption of NH_3 [kcal/mol]
d_j	Pores mean diameter [Å]
d_h	Hydraulic diameter of the monolith channel [cm]
D_i	Molecular diffusion coefficient of i-th species [cm^2/s]
$D_{eff,i}$	Effective diffusion coefficient of i-th species [cm^2/s]
$D_{K,j}$	Knudsen diffusion coefficient [cm^2/s]
ε_j	Porosity (pore volume/catalyst volume) of micro or macro pores
ε_{TOT}	Total porosity
$E_{Att\ DeNO_x}$	Activation energy of the $DeNO_X$ reaction [kcal/mol]
$E_{Att\ Hg}$	Activation energy of the Hg^0 oxidation reaction [kcal/mol]
η	Effectiveness factor for $DeNO_X$ reaction
η_{Hg}	Effectiveness factor for Hg oxidation reaction
θ_{NH_3}	Surface coverage of NH_3
h	Half thickness of the catalytic wall [cm]
k_{DeNO_x}	Intrinsic rate constant of the $DeNO_X$ reaction [1/s]
k_{Hg}	Intrinsic rate constant of the Hg^0 oxidation reaction [1/s]
$k_{mt,i}$	Gas–solid mass transfer coefficient of i-th species [cm/s]
K_{NH_3}	Adsorption constant of NH_3 [cm^3/mol]
$K^*_{NH_3}$	Dimensionless adsorption constant of NH_3 = $K_{NH_3}C^0_{NO}$
K_{NH_3Hg}	NH_3 inhibition constant in Hg^0 oxidation [cm^3/mol]
$K^*_{NH_3Hg}$	Dimensionless NH_3 inhibition constant in Hg^0 oxidation = $K_{NH_3Hg}C^0_{NO}$
L	Reactor axial length [cm]
μ	Gas dynamic viscosity [Pa·s]
ρ	Catalyst bulk density [g/cm^3]
ρ_g	Gas density [g/cm^3]
R	Dimensionless group in Eq. (9)
Re	Reynolds number = $\rho_g v d_h/\mu$
s	Wall half thickness [cm]
Sc	Schmidt number = $\mu/\rho_g D_{Hg}$
Sh_i	Sherwood number = $k_{mt,i}d_h/D_i$
v	Gas velocity [cm/s]
Φ_i	Thiele number of i-th species
x	Transverse intraporous coordinate [cm]
x^*	Normalized transverse intraporous coordinate = x/s
z	Axial coordinate [cm]
z^*	Graetz coordinate
Z	Normalized Z-coordinate = z/L

Subscripts and superscripts

b	Gas bulk phase
w	Gas–solid interface
m	Micropores d < 400 Å
M	Macropores d > 400 Å

due to its high volatility and low solubility in water [6,9]. This is the reason why, at present, none of the existing separation technologies can guarantee the target of 90% abatement of elemental mercury, as ruled in December 2011 by the Environmental Protection Agency [3].

Among all the technologies, catalytic oxidation of elemental mercury to ionic mercury, combined with ESP/FF and/or wet scrubbing, is presently the most promising method to achieve, in a cost effective way, such a target [1]. The literature on catalytic oxidation of mercury has flourished in recent years; several oxidation catalysts have been studied and reported to be highly active including noble metals [10–12], transition metal catalysts [13–16] and, most interestingly, SCR catalysts [17,18]. Indeed, it is now well known from lab-scale studies and confirmed by field tests that the presence of a SCR-$DeNO_X$ unit affects mercury speciation since the SCR catalyst favors the highly desired conversion of Hg^0 to the ionic species Hg^{2+} in the presence of HCl in the flue gas; in the literature the reaction is usually referred to as *oxidation* of elemental mercury to ionic mercury, but in practice it is an *oxi-chlorination* of Hg^0, with stoichiometry:

$$Hg^0 + 2HCl + 1/2O_2 \rightarrow HgCl_2 + H_2O \quad (1)$$

Several studies have investigated the reaction over V_2O_5–WO_3/TiO_2, mostly with emphasis on catalyst and reactor performances. A number of macroscopic kinetic effects have been unanimously recognized in the scientific and technical literature. It is for instance well known that under typical SCR conditions the conversion of Hg^0 increases with increasing V-content of the catalyst [17], thus V-sites are believed the active sites of the reaction. Also, it has been reported that the rate of Hg^0 oxidation is negligible in the absence of HCl (in which case adsorption and surface accumulation of mercury-species occur [19,20]) and it proceeds at high rates in the presence of HCl [21]. Several authors have shown that the promoting effect of HCl concentration has an asymptotic trend when explored in a wide concentration range [17,22–25]; this is in line with the proposal that the active site is a chlorinated V-site [21] or with the more general assumption that the reaction requires adsorption of HCl to generate Cl-surface species that react with gas-phase or weakly bound Hg^0 [26–28].

The temperature dependence of Hg^0 conversion is typically reported as moderate or even negative at temperatures above 380 °C [22,26,29,30]; this effect has not been fully explained in the literature, and assumptions have been made on the limiting role of adsorption steps. External mass transfer limitations could explain low values of the apparent activation energy, in analogy with the case of the SCR reaction [26]. However, Madsen et al. [31,32] have recently shown, by running experiments over a proprietary V-based catalyst at low space velocity and comparing them with thermochemical equilibrium calculations, that the oxi-chlorination of Hg^0 (1) is a reversible process and the thermodynamics are such that Hg^0 is the favored species at high temperatures. Indeed the impact of thermodynamics on the speciation of mercury is well known in the literature of gas-phase chemistry in incinerators and burners [33–35]. Thus, the moderate or even reverse temperature dependence of Hg^0 conversion could be partly associated with the approach to thermodynamic equilibrium.

Finally, it is widely recognized that Hg^0 oxidation is inhibited by NH_3 [18,20,22,25,29,36,37]. This effect has been mostly explained by invoking a competitive adsorption of NH_3 on the active sites. Madsen et al. [31,32] have better shown that the inhibition is typical of low to medium reaction temperatures, while over 325 °C NH_3 apparently acts as a reducing agent for $HgCl_2$. Stolle et al. [25] have recently confirmed from combined $DeNO_X$ and Hg-oxidation tests over SCR monoliths that ammonia can effectively reduce $HgCl_2$ to elemental mercury at 390 °C.

All these phenomena suggest a certain complexity of the catalytic process, but a clear kinetic and mechanistic interpretation

(including the identification of the elementary reaction scheme, the nature of the catalytic site, the nature of the intermediate species and of the rate determining steps) is still missing. The fundamentals of the interaction of mercury and chlorine species on V-based catalysts are however being addressed in the recent literature by the means of DFT analyses [38–40].

In this work, we focus on the impact of ammonia inhibition on Hg^0 oxidation in reaction (1). As mentioned by Niksa and Sibley [41], the existence of NH_3 inhibition suggests an analogy between the Hg^0 oxidation process and the SO_2–SO_3 process investigated in previous studies [42]. The extent of such an inhibition is differently reported in the literature. Niksa and Sibley [41] have reported Hg^0 conversion measurements from a full scale reactor wherein mercury conversion moderately decreased (from 85% to 65%) at increasing NH_3/NO feed ratio from 0 to 0.95. A more pronounced effect was reported by Niksa and Fujiwara [26], who observed a decrease of Hg^0 conversion from 85 to about 40% at increasing NH_3/NO ratio. Kamata et al. [17] observed instead a dramatic effect and reported the loss of Hg^0 conversion efficiency from 80% to 0% at increasing NH_3/NO feed ratio. The scatter among data, though obtained at comparable values of space velocity and temperature, can be partially explained by possible differences in the nature of coals, which affects the composition of the flue gases and in particular the concentration of HCl and the content of fly ashes. And these factors can in turn affect the surface chemistry but also the accuracy of the speciation measurement, highly critical because of the inherent complexity of the analysis.

Thus, given on one side the importance of comprehending the impact of ammonia inhibition on the performance of the reactor, and on the other side the scatter but also the uncertainty of the available experimental measurements, in this work we looked for a chemical engineering analysis of the phenomenon, in order to better rationalize the ways and the extent of the interaction between ammonia adsorption and Hg^0 oxidation. At this scope we developed a model of the SCR reactor that incorporates the description of the diffusion and reaction processes inside the monolith wall; the model extends the mathematical treatment developed by Tronconi et al. [43,44], able to describe NO_X reduction and SO_2 oxidation in SCR reactors.

Few other studies have addressed the modeling of the SCR process, including Hg^0 oxidation. Kamata et al. [17] have reported a simplified plug flow model, which neglects the role of external and intraporous mass transfer limitations on both reactions. Thus the $DeNO_X$ and the Hg^0 oxidation performances were analyzed on the basis of apparent reaction rates. Niksa and Fujiwara [26] have first decoupled the contribution of external diffusion resistances on Hg^0 oxidation by developing a heterogeneous 1D model, which has been applied to describe a wide range of data sets from lab-scale, to pilot scale and full scale plants. Later, Niksa and Sibley [41] have proposed a complete mathematical treatment that incorporates the $DeNO_X$ and SO_2–SO_3 model of Tronconi et al. [44] and adds to it a description of the Hg^0 oxidation process which incorporates a simplified expression of the effectiveness factor. The model was applied to simulate several full scale data and analyze the potential for an improvement of Hg^0 conversion by modification of the macropore void fraction. Emphasis was thus on the integral performance of the reactor.

With a more fundamental approach, in this work, we focus on the specific roles that external and internal diffusion resistances have on the extent of NH_3 inhibition; since ammonia concentration drops to zero within a very thin surface catalyst layer, due to the diffusion controlled kinetics of the $DeNO_X$ process, it may be expected that inter- and intra-phase mass transfer limitations will have an important role in determining the impact of ammonia on the rate of Hg^0 oxidation. Accordingly we herein take a close look at the intraporous field and analyze parametrically which factors mainly affect the shape of the concentration profiles within the monolith wall, as a means to rationalize the phenomena observed at the macro-scale of the reactor. According to the recent findings by Haldor Topsoe [31,32] and Koeser and coworkers [25], the treatment herein proposed (wherein ammonia is uniquely consumed by the $DeNO_X$ reaction and mercury oxidation is a forward reaction) applies rigorously to conditions where the approach to thermodynamic equilibrium or possible reactions of $HgCl_2$ with ammonia are negligible, thus for temperatures below 350 °C.

The paper consists of three main sections: we first illustrate the model equations, discussing the assumptions and the rate expressions herein implemented, then we estimate the characteristic kinetic parameters of the kinetic scheme from independent data (both at the lab-scale and at the pilot-scale) and verify the model adequacy against pilot scale data, finally we apply the model to analyze the concentration and rate profiles inside the reactor for typical catalyst and reactor conditions and address a parametric study.

2. Experimental

2.1. Catalysts

Commercial High Dust catalysts were tested in the pilot reactor. The catalysts have a titanium dioxide (TiO_2) matrix honeycomb type, activated with vanadium pentoxide (V_2O_5) and tungsten trioxide (WO_3). Data on V-loading were provided by the producers and are reported in Table 1, together with the geometrical parameters of the monoliths.

For each catalyst, the pore size distribution curve was determined by combining the N_2 adsorption–desorption isotherm and the Hg-intrusion measurement on fragments of the monoliths.

2.2. Pilot scale tests on a power-plant stream line

Measurements of NO_X and Hg^0 conversions were obtained from a stream line at the Enel coal fired power plant in La Spezia (Italy). La Spezia Unit #3 is a 600 MW front coal-fired dry-bottom boiler. The boiler is equipped with an over firing air system (2 levels) and low-NO_X burners. The power unit burns a blend of bituminous coals. The first flue gas cleaning device is a high dust $DeNO_X$-SCR reactor. The SCR reactor consists of three catalyst layers of an overall volume of 535 m^3. A more detailed description of the plant layout is given in the Appendix. A side-stream reactor is installed in correspondence with on the first catalyst layer of the full-scale SCR-$DeNO_X$ unit. A slip stream (30–200 m^3/h STP) is taken from the flue gas duct downstream from the NH_3 injection and mixing system and is re-injected in the reactor below the first catalyst layer. A scheme of the side stream reactor is also provided in the Appendix, Fig. A1. The catalyst chamber is located in a thermostatic cell to maintain real flue gas temperature while the pipes and the fan are insulated and electrically heated. Two segments of commercial honeycomb monoliths ($0.15 \times 0.15 \times 0.25$ m each) are tested in the cell, arranged in series. The flow rate through the cell is regulated by the mass flow controller acting on a valve located on the reactor bypass: this allows changing the SV between 3400 and 27,000 1/h [45]. No ammonia flow rate control is operated

Table 1
V_2O_5 load and geometrical properties of the high-dust honeycomb monoliths.

	Cat. A	Cat. B	Cat. C	Cat. D	Cat. E
V_2O_5 [% w/w]	0.3	0.6	0.6	1.3	0.6
Pitch [mm]	6.63	7.00	7.11	6.81	7.10
Channel opening [mm]	5.65	6.12	6.31	6.04	6.45

and the (NH_3/NO_X) feed ratio in the pilot reactor is the same as in the full scale $DeNO_X$ unit.

Sampling ports are located upstream and downstream (an additional sampling point is located between the two segments) that allow analysis of the inlet and outlet concentration of NO and O_2 as well as the speciation of mercury (Hg^0, Hg^{2+}). NO and O_2 are measured, respectively, by a non-dispersive infrared (NDIR) method and a paramagnetic one. NH_3 is measured only downstream the catalyst at least twice for each experimental condition by an UV spectrometer, using a calorimetric analysis with Nessler reagent. The inlet ammonia is monitored by NH_3/NO feeding ratio of full-scale reactor (recorded data by plant information system). Mercury speciation is measured by an on-line monitoring system developed by ENEL Research based on a modified Ontario Hydro method [46,47]; a detailed description is provided in the SI.

Catalyst A–D were tested in the stream-line pilot reactor, collecting simultaneously data of NO conversion and Hg^0 conversion. The catalysts were conditioned in the side-stream reactor for a time period of 70–100 h under working conditions, before conversion measurements were made.

The gas stream typically contained 300–500 ppm NO_X, 500–1000 ppm SO_2, 20–40 ppm HCl, about 10% H_2O, 9% CO_2 and 4% O_2.

2.3. Hg^0–Hg^{2+} tests on monoliths in lab-scale reactor

The laboratory apparatus consists of three main sections (1) flue gas generation system; (2) catalytic cell; (3) measuring section. The synthetic flue gas mixture is chosen to simulate the gas composition typical of coal combustion without ash. The flue gas is obtained by mixing different components coming from high pressure cylinders (NO, SO_2, O_2, CO_2, NH_3, N_2). Hg^0 is fed in the vapor phase from a saturator maintained at 50 °C under N_2 flow. HCl is added, directly in the oven at 150 °C, to the reacting mixture upstream from the reactor by a peristaltic pump which fed a constant flow of 0.8 ml/min of aqueous solutions with varying HCl concentrations. All components are mixed together in the same oven at 150 °C. The Pyrex glass micro reactor is designed to hold one monolith catalyst sample ($20 \times 20 \times 400$ mm^3) and it is placed in an oven that can be heated up to 400 °C. A bypass system allows to measure on-line the flue gas composition (NO, SO_2, O_2, CO_2, NH_3, N_2, Hg^0, Hg^{2+}) alternatively upstream and downstream the catalyst. In particular, inlet and outlet mercury concentration is measured by a continuous mercury analyzer derived from a Perkin–Elmer Flow Injection Mercury System (FIMS). Finally, NO_X and SO_2 concentrations are analyzed by means of a NDIR spectrometer and O_2 content is evaluated thanks to a paramagnetic analyzer.

Small portions of Catalyst E, consisting of 3×3 channels elements with a total length of 20 cm, were cut from the commercial monolith module. The single catalyst element was placed in a cylindrical quartz reactor after tight wrapping in alumina cloth to avoid any by-pass; the reactor was then inserted in a heated chamber.

Reactivity tests were performed without any conditioning treatment of the catalyst: experimental data were collected when stationary Hg^0 conversion performances were reached.

2.4. $DeNO_X$ kinetic tests over powders

The intrinsic kinetics of the $DeNO_X$ reaction was measured for each catalyst in a micro flow reactor over powdered samples. The commercial monoliths were crushed into fine powders (<200 mesh), which, mixed with inert quartz particles (140–200 mesh), were packed in a quartz microreactor (9 mm of internal diameter). In the experiments, 30 mg of catalytic powders were diluted with quartz until reaching 5 mm of bed height. The reactor was placed in a furnace and the temperature was controlled by a thermocouple directly inserted in the catalytic bed. The simulated flue gas consisted of N_2, air, NO/He, NH_3/He, SO_2/He and CO_2, all supplied by high pressure cylinders and controlled by mass flow controllers (Brooks 5850); the supply of water was controlled by a liquid mass flow controller (Flomega 5881). N_2, air, CO_2 and water were mixed upstream from the oven, while NO, NH_3 and SO_2 were added directly inside the reactor and mixed with the feed steam throughout a bed packed with inert granular quartz, in order to ensure a uniform flow distribution. The quantitative detection of reactants and products was done by the use of an on-line FTIR analyzer (Multigas 2030, MKS). Catalytic samples were first pretreated at 450 °C in O_2 (2% in He with a total flow rate of 650 Ncm^3/min) for 2 h. The SCR activity tests were carried out with a total flow rate of 650 Ncm^3/min and a composition of 30 ppm of NO, 10 ppm of SO_2, 3.5% of O_2, 1% of CO_2 and 7% of H_2O in nitrogen. NH_3 was fed at two concentrations, 33 and 150 ppm to study the kinetic dependence of the $DeNO_X$ reaction from NH_3 adsorption. Temperature was randomly varied in between 250 and 400 °C, thus including typical industrial conditions.

3. Development of a 1D + 1D model of the reactor with solution of the intraporous field

Since the focus of the present study is the analysis of the effect of NH_3 on Hg^0 oxidation within the catalyst wall, we herein neglected SO_2 oxidation. This process also occurs within the monolith wall, and is inhibited by NH_3 adsorption, as illustrated in previous studies from our group [42]. The incorporation of the mass balances of SO_2 and SO_3 in the model is important for a complete description of the reactor performance but is not strictly necessary at this stage of the analysis since it does not interfere with the mass balances of NH_3 and Hg^0. The kinetics for Hg oxidation, presented in the following, are representative of a SO_2 content of 500–1000 ppm, as typical in coal fired power plants.

3.1. $DeNO_X$ process

In previous studies, Tronconi and Forzatti [48] and Tronconi et al. [43,44] have assessed the adequacy of a one-dimensional heterogeneous mathematical model for the description of the $DeNO_X$ process in SCR honeycomb reactors. The model incorporated an

Table 2
Reactor model equations for the $DeNO_X$ process.

Gas-phase mass balances:

$$\frac{d\Gamma_{NO}}{dz^*} = -4Sh_{NO}\left(\Gamma^b_{NO} - \Gamma^w_{NO}\right) \quad (2)$$

$$\frac{d\Gamma_{NH_3}}{dz^*} = -4Sh_{NH_3}\frac{D_{NH_3}}{D_{NO}}\left(\Gamma^b_{NH_3} - \Gamma^w_{NH_3}\right) \quad (4)$$

with $z^* = z\dfrac{z/d_h}{ReSc}$

with initial conditions:

$$\Gamma_{NO}|_{z^*=0} = 1 \quad (3)$$

$$\Gamma_{NH_3}|_{z^*=0} = \alpha \quad (5)$$

Gas–solid continuity equations:

$$Sh_{NO}\left(\Gamma^b_{NO} - \Gamma^w_{NO}\right) = \frac{D_{NH_3}}{D_{NO}}Sh_{NH_3}\left(\Gamma^b_{NH_3} - \Gamma^w_{NH_3}\right) \quad (6)$$

$$Sh_{NO}\left(\Gamma^b_{NO} - \Gamma^w_{NO}\right) = Da_{DeNO_X}\eta\frac{K^*_{NH_3}\Gamma^w_{NO}\Gamma^w_{NH_3}}{1 + K^*_{NH_3}\Gamma^w_{NH_3}} \quad (7)$$

with effectiveness factor η, developed by Tronconi et al. [42] for Eley Rideal kinetics in a slab:

$$\eta = \frac{\sqrt{R}}{\Phi}\frac{1}{\frac{K^*_{NH_3}\Gamma^w_{NO}\Gamma^w_{NH_3}}{1+K^*_{NH_3}\Gamma^w_{NH_3}}} \quad \text{with} \quad \Phi = s\sqrt{\frac{k_{DeNO_X}}{D_{eff,NO}}} \quad (8)$$

$$R = \Gamma^{w2}_{NO} - \Gamma^2_{NO,0} + 2(S_1 - S_2)\left(\Gamma^w_{NO} - \Gamma_{NO,0} - S_2\ln\frac{\Gamma^w_{NO} + S_2}{\Gamma_{NO,0} + S_2}\right) \quad (9)$$

$$S_1 = \frac{D_{eff,NH_3}}{D_{eff,NO}}\Gamma^w_{NH_3} - \Gamma^w_{NO} \quad (10)$$

$$S_2 = S_1 + \frac{D_{eff,NH_3}}{D_{eff,NO}}\cdot\frac{1}{K^*_{NH_3}} \quad (11)$$

$$\Gamma_{NO,0} = -S_1 \quad \text{or} \quad \Gamma_{NO,0} = 0 \quad \text{if} \quad S_1 > 0 \quad (12)$$

estimate of the local Sherwood number based on the analogy of the gas–solid mass transfer with the Greatz problem of heat transfer in square channels with constant temperature; it described the reaction at the wall with an Eley Rideal rate expression and accounted for the impact of intraporous mass transfer limitations through an analytical solution of the effectiveness factor (valid for the Eley Rideal kinetics) for slab geometry. The same lumped model was herein adopted and is reported in Table 2, Eqs. (2–12), for the sake of clarity. This system of equations provides a complete characterization of the process in terms of axial evolution of the concentration of reactants in the bulk phase and at the bulk-solid interface, provided that the geometrical properties, the pore size distribution and the kinetic parameters for the DeNO$_X$ reaction are known.

In addition to it, in order to make available the detailed description of NO and NH_3 intraporous concentration profiles, we addressed the treatment of the intraporous field; first we solved numerically the reaction and diffusion problem within the monolith wall (which has not been reported for the sake of brevity) and then we developed approximate analytical solutions of the intraporous concentration profiles. These are shown in Table 3, Eqs. (13–16), and represent a complement of the lumped DeNO$_X$ model in Table 2.

Such analytical solutions assume the well known form for pseudo-first order kinetics:

$$C_i(x) = C_{i,w}\frac{\cosh(\Phi_i x)}{\cosh(\Phi_i)}$$

where i = NO or NH_3 is the limiting reactant within the wall and the modified Thiele modulus Φ_i is defined as:

$$\Phi_i = h\sqrt{\frac{r_{\mathrm{DeNO_X}/C_{i,w}}}{D_{eff,i}}}$$

In other words, it is assumed that the Eley–Rideal reaction rate:

$$r_{\mathrm{DeNO_X}} = k_{\mathrm{DeNO_X}} C_{\mathrm{NO}}\frac{K_{\mathrm{NH_3}}C_{\mathrm{NH_3}}}{1+K_{\mathrm{NH_3}}C_{\mathrm{NH_3}}}$$

can be reduced either to a first order dependence on NO concentration ($r_{\mathrm{DeNO_X}} \propto C_{\mathrm{NO}}$) when NO is the limiting reactant within the wall, or to a first order dependence on NH_3 concentration ($r_{\mathrm{DeNO_X}} \propto C_{\mathrm{NH_3}}$) when NH_3 is the limiting reactant within the monolith wall.

To evaluate which simplifying assumption (either pseudo-first order in NO or pseudo-first order in NH_3) applies at a generic axial coordinate z, the model compares the "potential" to intraporous diffusion of the two reactants by evaluating the ratio:

$$\frac{D_{eff,\mathrm{NO}}C_{\mathrm{NO},w}}{D_{eff,\mathrm{NH_3}}C_{\mathrm{NH_3},w}}$$

where $D_{eff,i}$ and $C_{i,w}$ are the effective diffusion coefficient and the concentration at the gas–solid interface of the i-th reactant.

$$\text{If}\quad \frac{D_{\mathrm{NO},eff}C_{\mathrm{NO},w}}{D_{\mathrm{NH_3},eff}C_{\mathrm{NH_3},w}} > 1$$

then it is assumed that NH_3 is the limiting reactant; otherwise, NO is treated as the limiting reactant.

The adequacy of such approximate treatment was verified by comparison with the solution of the rigorous problem of diffusion and reaction for NH_3 and NO inside the monolith wall, at varying NH_3/NO ratio and AV. For the sake of brevity we omit examples of such a comparison; the match was highly satisfactory.

3.2. Hg^0 oxidation

The model equations, necessary to describe the oxidation of Hg^0 in the monolith channel, are reported in Table 4.

In analogy with the DeNO$_X$ process and in line with Niksa and Fujiwara [26] and Niksa and Sibley [41], a lumped approach was adopted to describe the mass balance of Hg^0 in the gas phase, Eqs. (17–18). Concerning the intraporous field, the second order differential mass balance (Eq. 19) was solved in combination with the boundary conditions at the gas–solid interface (continuity of the flow, Eq. 20) and at half thickness of the wall (symmetry of the concentration profile, Eq. 21). Orthogonal collocations were used to solve the profiles along the intraporous coordinate. Typically 14 collocation points were necessary to obtain numerical convergence.

Concerning the reaction kinetics, we adopted a rate expression of the form:

$$r_{\mathrm{Hgox}} = \frac{k_{\mathrm{Hg}}C_{\mathrm{Hg}}}{1+K_{\mathrm{NH_3Hg}}C_{\mathrm{NH_3}}}$$

where r_{Hgox} is the intrinsic rate per unit catalyst volume, k_{Hg} the intrinsic rate constant, and $K_{\mathrm{NH_3Hg}}$ the inhibition parameter of ammonia. A first order dependence on Hg^0 concentration was

Table 3
Reactor model equations for the DeNO$_X$ process: approximate description of the intraporous field.

If $\frac{D_{eff,\mathrm{NO}}\Gamma^w_{\mathrm{NO}}}{D_{eff,\mathrm{NH_3}}\Gamma^w_{\mathrm{NH_3}}} \leqslant 1$	then	
$\Gamma_{\mathrm{NO}} = \Gamma^w_{\mathrm{NO}}\frac{\cosh(\Phi_{\mathrm{NO}^w}x^*)}{\cosh(\Phi_{\mathrm{NO}^w})}$	$\Gamma_{\mathrm{NH_3}} = \Gamma^w_{\mathrm{NH_3}} + \frac{D_{eff,\mathrm{NO}}}{D_{eff,\mathrm{NH_3}}}(\Gamma_{\mathrm{NO}} - \Gamma^w_{\mathrm{NO}})$	(13–14)
If $\frac{D_{eff,\mathrm{NO}}\Gamma^w_{\mathrm{NO}}}{D_{eff,\mathrm{NH_3}}\Gamma^w_{\mathrm{NH_3}}} > 1$	then	
$\Gamma_{\mathrm{NH_3}} = \Gamma^w_{\mathrm{NH_3}}\frac{\cosh(\Phi_{\mathrm{NH_3^w}}x^*)}{\cosh(\Phi_{\mathrm{NH_3^w}})}$	$\Gamma_{\mathrm{NO}} = \Gamma^w_{\mathrm{NO}} + \frac{D_{eff,\mathrm{NH_3}}}{D_{eff,\mathrm{NO}}}\left(\Gamma_{\mathrm{NH_3}} - \Gamma^w_{\mathrm{NH_3}}\right)$	(15–16)
with $\Phi_{\mathrm{NO}^w} = \frac{h}{2}\sqrt{\frac{k_{\mathrm{DeNO_X}}\theta_{\mathrm{NH_3}}}{D_{eff,\mathrm{NO}}}}$;	$\Phi_{\mathrm{NH_3^w}} = \frac{h}{2}\sqrt{\frac{k_{\mathrm{DeNO_X}}\theta_{\mathrm{NH_3}}C^w_{\mathrm{NO}}}{C^w_{\mathrm{NH_3}}D_{eff,\mathrm{NO}}}}$;	$\theta_{\mathrm{NH_3}} = \frac{K^*_{\mathrm{NH_3}}\Gamma^w_{\mathrm{NH_3}}}{1+K^*_{\mathrm{NH_3}}\Gamma^w_{\mathrm{NH_3}}}$;
$x^* = \frac{x}{s}$		

Table 4
Reactor model equation for the Hg^0 oxidation process.

Gas-phase mass balance:

$$\frac{d\Gamma_{\mathrm{Hg}}}{dz^*} = -4Sh_{\mathrm{Hg}}(\Gamma^b_{\mathrm{Hg}} - \Gamma^w_{\mathrm{Hg}}) \quad (17)$$

with initial condition:

$$\Gamma_{\mathrm{Hg}}|_{z^*=0} = 1 \quad (18)$$

Solid-phase mass balance:

$$\frac{d^2\Gamma_{\mathrm{Hg}}}{dx^{*2}} = \Phi^2_{\mathrm{Hg}}\frac{\Gamma_{\mathrm{Hg}}(x)}{1+K^*_{\mathrm{NH_3Hg}}\Gamma_{\mathrm{NH_3}}(x)} \quad (19)$$

with boundary conditions:

$$\left.\frac{\Gamma_{\mathrm{Hg}}}{dx^*}\right|_{x^*=1} = Bi_{\mathrm{Hg}}\left(\Gamma_{\mathrm{Hg}} - \Gamma^w_{\mathrm{Hg}}\right) \quad (20)$$

$$\left.\frac{\Gamma_{\mathrm{Hg}}}{dx^*}\right|_{x^*=0} = 0 \quad (21)$$

with $\Gamma_{\mathrm{Hg}} = \frac{C_{\mathrm{Hg}}}{C^0_{\mathrm{Hg}}}$, $\Phi_{\mathrm{Hg}} = s\sqrt{\frac{k_{\mathrm{Hg}}}{D_{eff,\mathrm{Hg}}}}$, $Bi_i = Sh_i\frac{D_i}{D_{eff,i}}\frac{s}{d_h}$,

with effectiveness factor:

$$\eta_{\mathrm{Hg}} = \frac{\int_0^1 \Phi_{\mathrm{Hg}}\frac{\Gamma_{\mathrm{Hg}}(x)}{1+K^*_{\mathrm{NH_3Hg}}\Gamma_{\mathrm{NH_3}}(x)}dx^*}{\Phi_{\mathrm{Hg}}\frac{\Gamma^w_{\mathrm{Hg}}}{1+K^*_{\mathrm{NH_3Hg}}\Gamma^w_{\mathrm{NH_3}}}}} \quad (22)$$

assumed, in line with previous works in the literature; the proportionality of the reaction rate on Hg^0 concentration was experimentally verified as reported below. An inhibition term by NH_3 was also included in the denominator; such a term has a phenomenological character rather than a mechanistic one. It is noted, however, that this same form has been proposed and successfully applied by several authors to quantify the inhibiting effect of ammonia, based on the assumption of competitive adsorption on active sites according to either Eley–Rideal or Langmuir–Hinshelwood kinetics [17,27,41]. Notably, a very similar simplified form has been adopted also to render the inhibiting effect of ammonia on the oxidation of SO_2 to SO_3 [48].

At this stage of the work, we did not explicitly express a kinetic dependence of the reaction rate on the concentration of HCl.

Considering the compositions of the coals treated in the power plant during the experimental campaign, the parameters of the Hg^0 oxidation reaction estimated by fitting the pilot reactor data refer to an average HCl concentration within the range 20–40 ppm, where the reaction rate is expected to become less sensitive to HCl [24]; the qualitative dependence of the reaction rate on HCl content was experimentally verified in the lab-scale facility, as illustrated below.

The thermodymanics of Hg^0 speciation was analyzed to verify the possible approach to chemical equilibrium of the oxi-chlorination process under the operating conditions of the pilot reactor. It was verified that at temperatures of 300–310 °C the forward reaction is highly favored so that the ratio between the reaction quotient and the equilibrium constant:

$$\Pi^{p_i^{\nu_i}} \Big/ K_{\mathrm{eq}} \quad \text{is} \quad << 1$$

where in p_i is the partial pressure of the i^{th}-species and υ_i its stoichiometric coefficient.

This allows to treat the reaction as a simple forward reaction, thus neglecting the reversibility of the oxi-chlorination, which becomes important at higher temperatures. Fig. 1 shows the calculated mercury conversion at thermodynamic equilibrium, under typical flue gas conditions of the full scale plant and compares it with the measurements of Hg^0 conversion that were obtained over the different catalysts at low AV values. Equilibrium compositions were calculated by minimizing the Gibbs free energy of the reacting system and using thermochemical data from the NIST database [49].

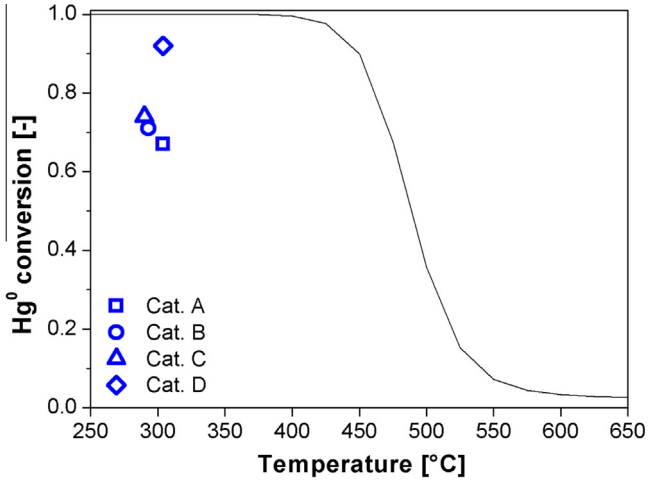

Fig. 1. Solid line: calculated conversion of elemental mercury in reaction R1 at the thermodynamic equilibrium. Simulated feed composition: Hg^0 = 10 μg/Nm^3; HCl = 21 mg/Nm^3; NO = 300 ppm; NH_3 = 300 ppm; SO_2 = 500 ppm; H_2O = 10%; O_2 = 5%; CO_2 = 9%; N_2 at balance. Symbols represent the measured conversions over the commercial catalysts A–D in the pilot scale tests at AV = 7 Nm/h.

Table 5
Mass transfer correlations.

Gas–solid mass transport correlation [50]:

$$Sh_i(z^*) = 2.977 + \exp(-57.2 \cdot z^*) \cdot 6.874 \cdot (1000 \cdot z^*)^{-0.488} \quad (23)$$

Molecular diffusion of Hg^0 [51]:

$$D_{\mathrm{Hg\text{-}N_2}} = 0.1211 \cdot \left(\frac{T}{273}\right)^{1.81} \quad (24)$$

(cm^2/s), 0–350 °C

Intraporous diffusion – Random Pore Model [52]:

$$D_{eff} = \varepsilon_M^2 D_M + (1-\varepsilon_M)^2 D_m + 2(1-\varepsilon_M)\varepsilon_M \frac{2}{\frac{1}{D_M}+\frac{1}{D_m}}$$

$$D_M = \frac{1}{\frac{1}{D_i}+\frac{1}{D_{K,M}}} \qquad D_m = \frac{\varepsilon_m^2/(1-\varepsilon_M)^2}{\frac{1}{D_i}+\frac{1}{D_{K,m}}}$$

3.3. Transport correlations

Transport properties were described with the correlations reported in Table 5.

As mentioned above, inter-phase mass transport was described by the correlation for the local Sherwood number with developing velocity and concentration profiles (Eq. (23)), whose adequacy has been widely discussed in the literature [26,50].

The binary molecular diffusion coefficients for NO and NH_3 in N_2 were calculated by the formula of Fuller et al. [51]. The molecular diffusion coefficient of elemental mercury was described by adopting the correlation proposed by Massman [52] Eq. (24), valid in the temperature range 0–350 °C.

Concerning the intraporous diffusion, for all the reacting species we adopted the Random Pore Model developed by Wakao and Smith [53] which describes the catalyst wall as an aggregate of microporous particles with interstices, representing the macroporosity, and the diffusion flow within the catalyst wall as a combination of molecular and Knudsen diffusion though micropores, through macropores and through macro and micro pores in series. We herein neglected the contribution of very large pores, with diameter >2000 Å.

4. Morphological characterization

Fig. 2 reports the cumulative pore volume curves of the four commercial catalysts; they were obtained by combining the Hg-adsorption curve and the N_2-desorption curve for each sample. The observed pore distributions are clearly the combination of various contributions.

Cat A and Cat B have a distinct bi-modal distribution with an important volume of mesopores (with average diameter of about 150 Å) and a contribution of macropores (with average diameter of 1000 Å). For Cat C and Cat D the decoupling of the contributions is difficult, being them very close in the range of mesopores: in these cases, the pore distributions have been treated as monomodal distributions. In all the samples a small volume was measured in correspondence with very large pores (around 10,000 Å) which are likely associated to small fractures or roughness on the monoliths geometric surface, visible by SEM inspection. Table 6 reports the discretization of the pores size distributions that have been used in the model for evaluating the effective diffusion coefficients (as illustrated below) as well as the surface areas of the catalysts. The calculated surface area values (assuming cylindrical pores) are in each case very close to the measured BET surface areas that are also reported in Table 6.

Using the correlations reported in Table 5 and the morphological data reported in Table 6, the diffusion coefficients of the reacting species were calculated at 573 K (Table 7). Notably, NH_3 molecular diffusivity in N_2 is comparable to NO molecular diffusivity; instead, the NH_3 effective diffusivity is about 30% higher than NO effective

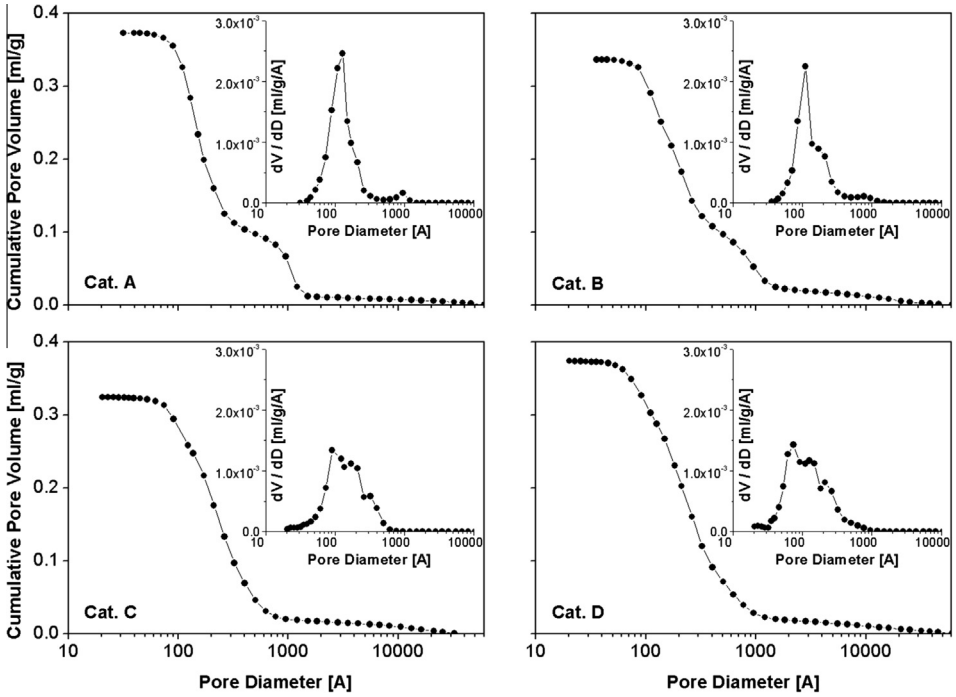

Fig. 2. Pore size distributions, obtained by the combination of Hg adsorption curves and N_2 desorption curves.

Table 6
Discretization of the pore size distribution.

	Cat. A	Cat. B	Cat. C	Cat. D	Cat. E
d_m [Å]	160	160	210	240	190
d_M [Å]	1000	900			1100
ε_m [-]	0.28	0.31	0.43	0.49	0.4
ε_M [-]	0.16	0.15			0.14
$\varepsilon_{TOT}(d < 10^5$ Å) [-]	0.44	0.49	0.46	0.52	0.55
ρ [g/cm^3]	1.38	1.53	1.37	1.34	1.51
$A_{sup,BET}$ [m^2/g]	54.5	53.1	60.1	60.9	63.26

diffusivity, due to the prevailing role of Knudsen diffusivity. Both in the gas phase and in the porous wall, Hg^0 diffusion is much slower (3–4 times) than the diffusion of the $DeNO_X$ reactants.

5. Parameter estimate by analysis of either kinetic tests on powders or tests on monoliths

5.1. $DeNO_X$ process

The kinetic constants of the NH_3-SCR reaction were independently estimated from experiments on powders. Fig. 3 shows as an example the results of the activity tests on catalyst B; these were performed at NO concentration of 30 ppm and NH_3 concentration of 33 and 150 ppm, at varying reaction temperature. The data were thus informative on the intrinsic kinetic constant and the activation energy of the SCR reaction, but also on the ammonia adsorption capacity and the heat of adsorption. An effect of ammonia concentration was in fact found, even under NH_3/NO ratios >1, because of the extremely low concentration of reactants.

Parameters were estimated by fitting a 1D pseudo-homogeneous reactor model (not reported for brevity); the model consisted of the mass balances for NO and NH_3 and incorporated the Eley Rideal kinetics. Model fit is also reported as solid lines in Fig. 3.

Kinetic and adsorption parameters are reported in Table 8. Notably, the estimates of K_{NH_3} and the estimates of the adsorption enthalpy were the same for the various catalysts, regardless of the different V-content. The parameters have been compared with those estimated in the past on analogous commercial catalysts from various providers, and a very good match was found [54].

Notably, as shown in Fig. 4, the estimates of k_{DeNO_X} at 300 °C form a systematic and approximately linear growing trend with increasing V load, as expected form the literature [54,55].

Based on the independent estimates of the kinetic parameters, the morphological properties of the catalysts and the geometrical data of the monoliths, the model of the reactor was applied to predict the pilot scale tests. Model predictions at varying AV are compared with the measurements of NO_X conversion in the stream line facility in Fig. 5. The validation was fully satisfactory for each commercial catalyst.

5.2. Hg^0–Hg^{2+} process

Estimates of the intrinsic kinetic constant for Hg^0 oxi-chlorination on catalysts A–D were obtained directly from the data col-

Table 7
Binary diffusion coefficients and effective diffusion coefficients at 300 °C.

	Cat. A	Cat. B	Cat. C	Cat. D	Cat. E
D_{NO} [cm^2/s]			7.60×10^{-1}		
D_{NH_3} [cm^2/s]			7.18×10^{-1}		
D_{Hg} [cm^2/s]			4.63×10^{-1}		
$D_{eff,NO}$ [cm^2/s]	1.17×10^{-2}	1.17×10^{-2}	1.17×10^{-2}	1.17×10^{-2}	1.17×10^{-2}
D_{eff,NH_3} [cm^2/s]	1.48×10^{-2}	1.48×10^{-2}	1.48×10^{-2}	1.48×10^{-2}	1.48×10^{-2}
$D_{eff,Hg}$ [cm^2/s]	4.72×10^{-3}	4.72×10^{-3}	4.72×10^{-3}	4.72×10^{-3}	4.72×10^{-3}

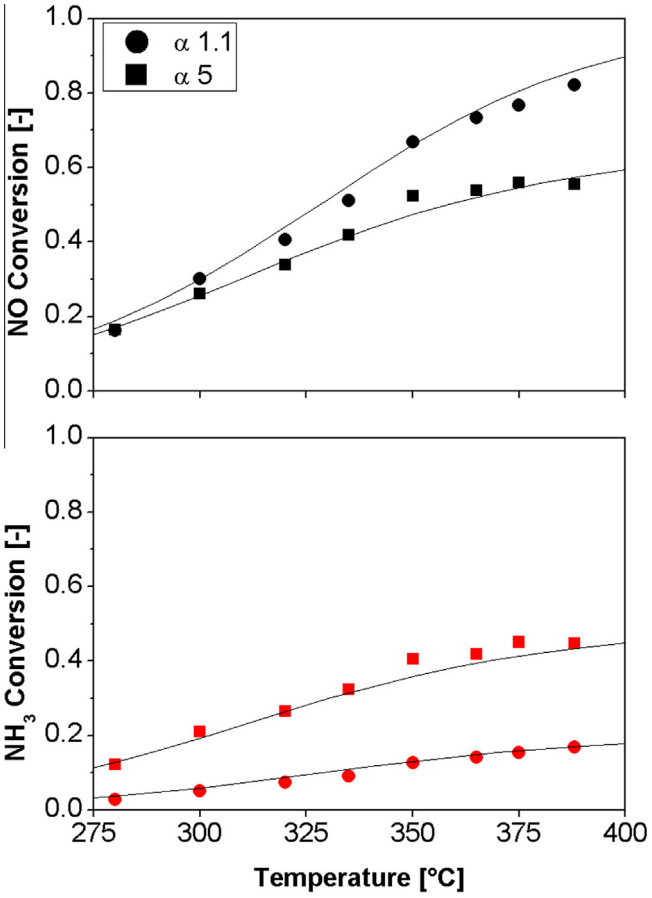

Fig. 3. NH_3-SCR lab-scale tests on powders, Cat B. Symbols: measured NO and NH_3 conversion at two values of NH_3/NO ratio. Feed composition: NO = 30 ppm; NH_3 = 33–150 ppm; SO_2 = 10 ppm; H_2O = 7%; O_2 = 3.5%; CO_2 = 1%; N_2 at balance. Solid lines: fit of the experimental data.

lected at the stream line facility; the complete reactor model (equations in Table 4) was adapted to the measured conversions of Hg^0, taking into account the simultaneous occurrence of the $DeNO_X$ process. Data and quality of the model fit are reported in Fig. 6.

Since all the available tests refer to NH_3/NO inlet ratios equal to or lower than 0.8 (the operating condition of the full scale SCR reactor in the power plant), no specific piece of information was available to estimate the kinetic dependence of Hg^0 oxidation on NH_3 concentration. We set the dimensionless parameter $K^*_{NH_3}$ in Eq. (8,15) to the reference value of 50,000, which is the same parameter value that was introduced to account for the inhibiting effect of ammonia on SO_2–SO_3 oxidation in previous works [48].

Given the complexity and relatively high uncertainty of the mercury analysis the match in Fig. 6 is satisfactory. Table 8 reports the estimates of the intrinsic rate constants at 300 °C for the various catalysts under study; they are also plotted in Fig. 7 and show a systematic increasing trend at increasing V content of the catalysts.

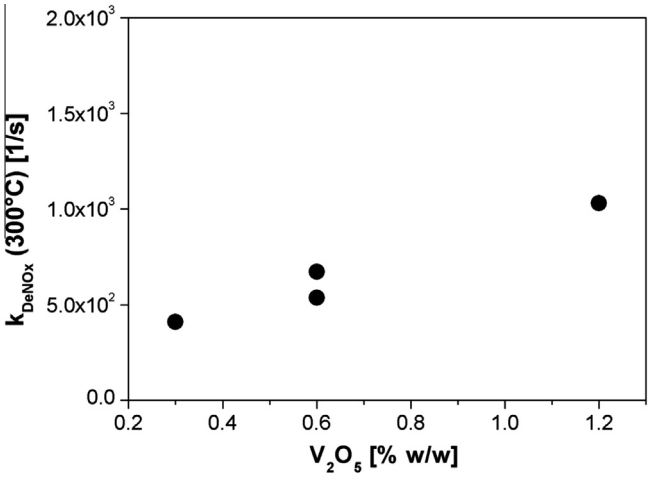

Fig. 4. Estimates of the intrinsic $DeNO_X$ contant k_{DeNO_X} (calculated @ 300 °C) vs V_2O_5 load.

A further support to the kinetic analysis was provided by the activity tests on catalyst E, performed on 3 × 3 channels monoliths in the testing unit at the Enel labs. Experiments were performed at the AV value of 14 Nm/h at varying temperature, HCl concentration and Hg^0 concentration. Fig. 8a reports the measured effect of varying HCl concentration from 5 to 80 mg/Nm^3. It was found that the promoting effect of HCl is almost linear at low HCl concentration, but becomes moderate at higher concentrations, close to those typical of the the full scale and pilot scale reactor (that is HCl concentration higher than 10 mg/Nm^3); here the residual promoting effect of HCl appears comparable with the experimental uncertainty of the pilot scale facility. The experiments at varying Hg^0 concentration (Fig. 8b) showed nearly constant values of conversion, which supports the assumption in Eq. (17) of first order dependence of the reaction rate on mercury concentration, in line with several previous studies [17,26,41].

The data on the effect of temperature (Fig. 9) were exploited to obtain an independent estimate of the activation energy. This amounted to 21 kcal/mol; such an estimate could be obtained because of the capability of the model to decouple the effect of interphase mass transfer in the monolith channels and chemical reaction at the wall. This activation energy well compares with the value of 18 kcal/mol estimated by Eswaran and Stenger [22] over honeycomb monoliths at temperatures below 375 °C.

The same activation energy was assumed for Catalysts A–D.

Though smaller, the estimated intrinsic reactivity of catalyst E at 10 mg/Nm^3 HCl can be reasonably compared with the reactivity of the catalysts B and C (measured under real feed conditions in the stream line reactor). Fig. 9 shows in dotted line the prediction of Hg^0 conversion under the temperature and AV conditions of the lab-scale facility, but assuming the intrinsic reactivity of catalyst B. The predicted conversions are about 7–10% higher than those measured on catalyst E; however, based on the measured effect of HCl concentration (Fig. 8a), such a gap is fully coherent with

Table 8
Estimates of the kinetic parameters.

	Cat. A	Cat. B	Cat. C	Cat. D	Cat. E
k_{DeNO_X} (300 °C) [1/s]	$4.09{\cdot}10^2$	$5.36{\cdot}10^2$	$6.72{\cdot}10^2$	$1.03{\cdot}10^3$	$3.13{\cdot}10^2$
$E_{Att\ DeNO_X}$ [kcal/mol]	20	19	20	18	23
k_{Hg} (300 °C) [1/s]	$2.46{\cdot}10^2$	$4.01{\cdot}10^2$	$5.71{\cdot}10^2$	$3.80{\cdot}10^3$	$1.25{\cdot}10^1$
$E_{Att\ Hg}$ [kcal/mol]	21	21	21	21	21
K_{NH_3} (300 °C) [cm^3/mol]	$3.76{\cdot}10^9$	$3.76{\cdot}10^9$	$3.76{\cdot}10^9$	$3.76{\cdot}10^9$	$3.76{\cdot}10^9$
ΔH_{NH_3} [kcal/mol]	-20	-17	-17	-17	-10
K_{NH_3Hg} (300 °C) [cm^3/mol]	$2.35{\cdot}10^9$	$2.35{\cdot}10^9$	$2.35{\cdot}10^9$	$2.35{\cdot}10^9$	$2.35{\cdot}10^9$

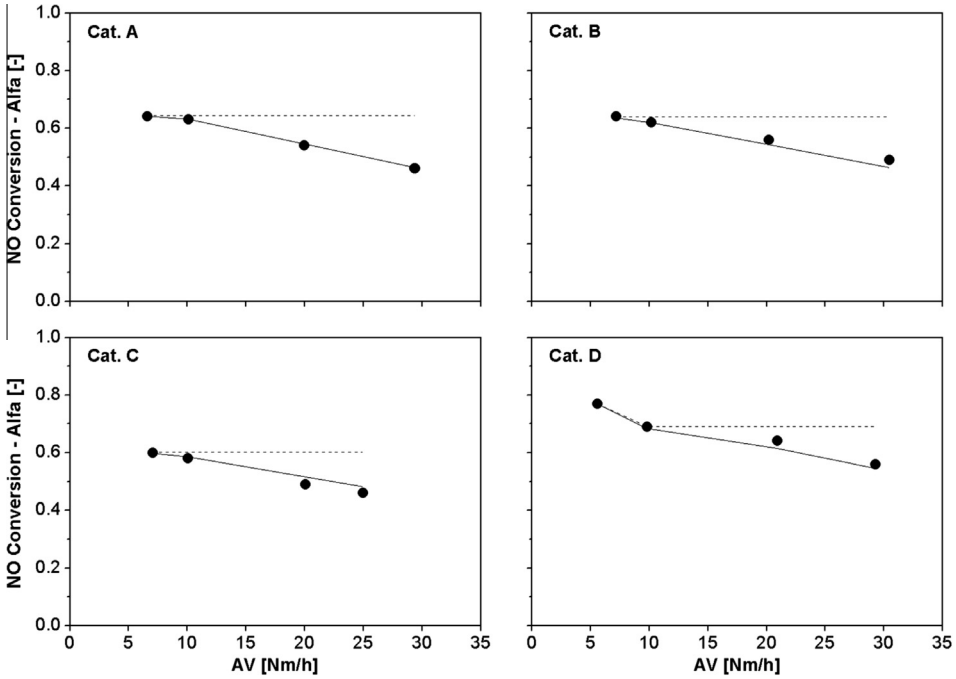

Fig. 5. Experimental campaign on monoliths, stream line reactor. T = 310 °C, NO concentration = 350 ppm. Symbols: measured NO conversion at varying AV. Dotted lines: values of the inlet NH_3/NO ratio measured in the stream line. Solid lines: model predictions.

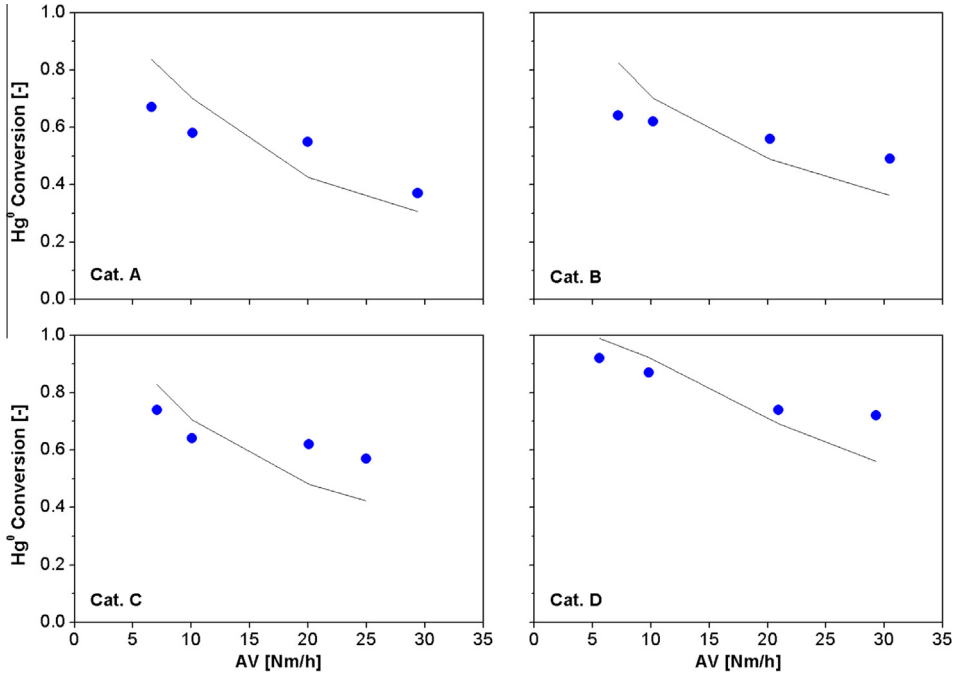

Fig. 6. Experimental campaign on monoliths, stream line reactor. Symbols: measured Hg^0 conversion at varying AV. Solid lines: model simulations.

the difference of HCl concentration (10 mg/Nm^3 vs. likely >20 mg/Nm^3) between the tests in the lab-scale facility and the tests in stream line facility.

6. Analysis of the reactor performance under reference conditions

It is now interesting to examine more closely the performance of the whole reactor and specifically to take a close look at the concentration profiles of all the reactants along the channels and inside the monolith wall. Fig. 10 plots the predicted axial conversion profiles of NO, NH_3 and Hg^0 for the four catalysts tested in the pilot scale reactor, at AV = 7 Nm/h and alpha = 0.8, that is under typical operating conditions of the full scale reactor.

The evolution of the conversion profiles show that the $DeNO_X$ process starts at an higher rate than Hg^0 oxidation, over all catalysts; this is due to the different intrinsic rates of the chemical processes, and partly to the inhibiting effect of NH_3 on Hg^0 oxidation that is especially important at the reactor inlet, where NH_3 concen-

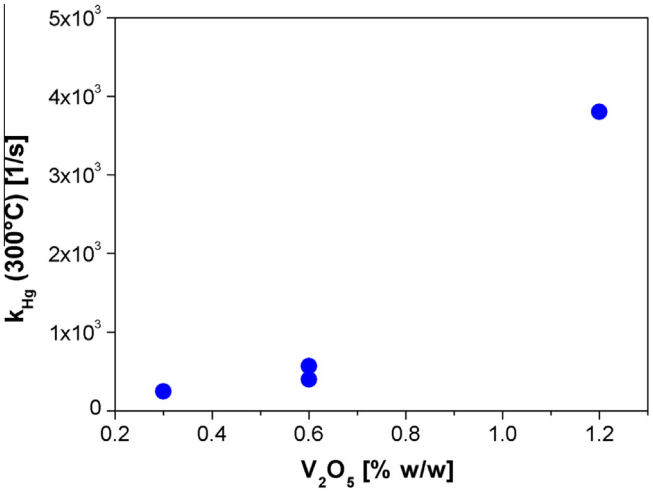

Fig. 7. Estimates of the intrinsic Hg^0 oxidation constant k_{Hg} (calculated @ 300 °C) vs V_2O_5 load.

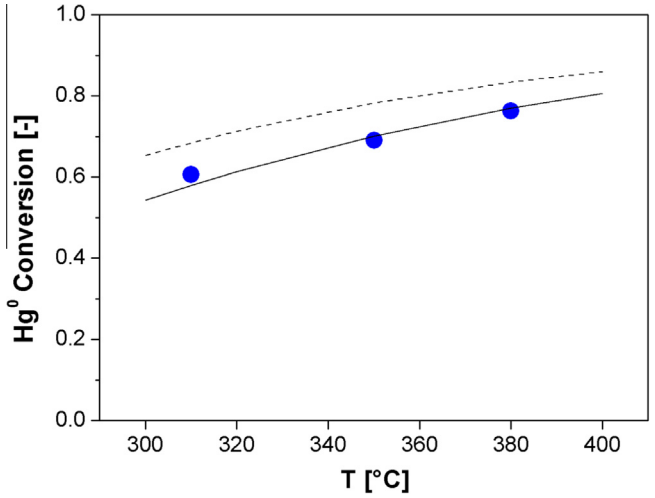

Fig. 9. Symbols: measured effect of temperature on Hg^0 conversion for Catalyst E. Feed composition: Hg^0 = 10 μg/Nm^3; HCl = 10 mg/Nm^3; NO = 300 ppm; SO_2 = 500 - ppm; H_2O = 10%; O_2 = 5%; CO_2 = 9%; N_2 at balance. Solid line: model fit and estimation of activation energy (k_{Hg} = 1.7 × 10^2 1/s; $E_{ATT\ Hg}$ = 21 kcal/mol). Dotted line: expected performance of catalyst B under the same test conditions of catalyst E (k_{Hg} = 4.01 × 10^2 1/s; $E_{ATT\ Hg}$ = 21 kcal/mol).

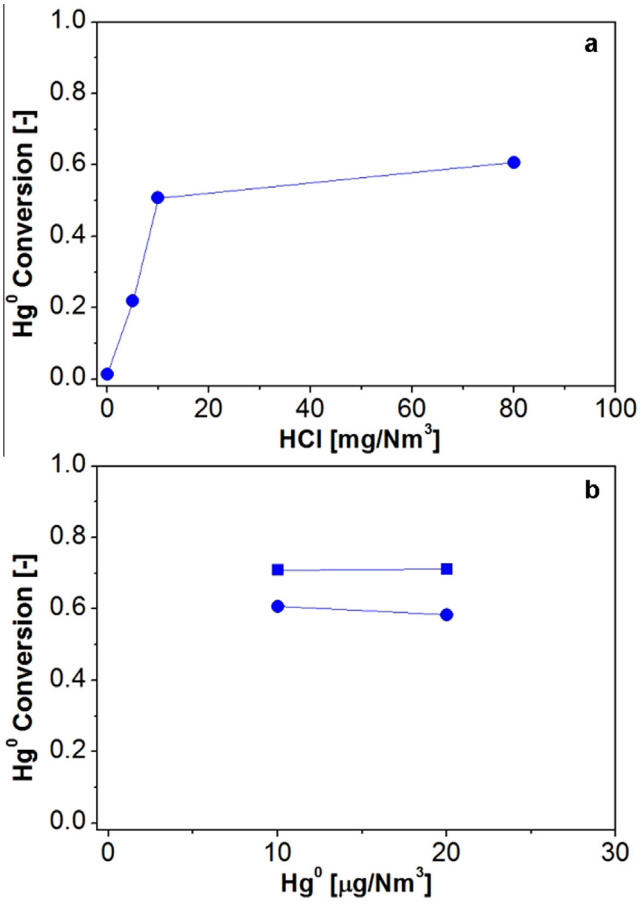

Fig. 8. (a): Measured effect of HCl feed content on Hg^0 conversion for Catalyst E at 310 °C, AV = 14 Nm/h. Feed composition: Hg^0 = 10 μg/Nm^3; NO = 300 ppm; SO_2 = 500 ppm; H_2O = 10%; O_2 = 5%; CO_2 = 9%; N_2 at balance. (b): Measured effect of Hg^0 feed content on Hg^0 conversion for Catalyst E at 310 °C, AV = 14 Nm/h. Feed composition: HCl = 10 (circles) – 80 (squares) mg/Nm^3; NO = 300 ppm; SO_2 = 500 - ppm; H_2O = 10%; O_2 = 5%; CO_2 = 9%; N_2 at balance.

tration is high. Considering the whole reactor length, however, it is noted that while most of the $DeNO_X$ process occurs within the first half of the reactor, as long as NH_3 is available, Hg^0 consumption proceeds along the whole reactor length because of the absence of any stoichiometric constraint. For the same reason, while at AV = 7 Nm/h there is no integral effect of the V-loading on the $DeNO_X$ efficiently (fully controlled by the stoichiometry), the axial Hg conversion profiles significantly grow at increasing V-content from catalyst A, to catalysts B and C, to catalyst D.

Concerning the impact of external mass transfer limitations, Fig. 11 shows, for the case of Catalyst B, the calculated axial profiles of concentration in the bulk and at the gas–solid interface (indicated with the subscript "wall" in the figure) for the various reactants. The kinetic role of gas–solid diffusion, as well known in the literature, is very important in the case of the $DeNO_X$ process which proceeds under a mixed diffusion-chemical regime; in fact, in Fig. 11 the calculated concentration of NH_3 (the limiting reactant) at the wall is much lower than the corresponding concentration in the bulk phase and drops very rapidly after the entry region of the reactor. For the case of Catalyst B, we calculate a Damköhler number of the $DeNO_X$ reaction of about 20 at 300 °C. Important, but less dramatic was found the impact of the external diffusion on the Hg^0 oxidation process, whose asymptotic Damköhler number (evaluated conservatively at the outlet of the reactor, where the inhibiting effect of NH_3 is negligible) is about 12; the calculated concentration of Hg^0 at the wall in Fig. 11 is in fact lower than the bulk phase concentration, but always significantly higher than zero.

Fig. 12 analyzes the impact of intraporous diffusion limitations; here the radial concentration profiles of NO, NH_3 and Hg^0 are calculated at different axial coordinates, assuming an AV value of 21 Nm/h; this corresponds to the flow conditions of the first layer in a full scale reactor, which typically operates at AV = 7 Nm/h. At the same axial coordinates, the right hand panels of Fig. 12 also show the calculated radial profiles of the Hg^0 oxidation rate. It is found that both NH_3 concentration and Hg^0 concentration drop to zero within a thin superficial catalyst layer. Since the intensity of the inhibition decreases with the decreasing concentration of ammonia, the rate of Hg^0 oxidation presents a maximum at some distance from the gas–solid interface. Such a maximum tends to increase and shift towards the gas–solid interface with increasing z/L values, along with the progressive consumption of NH_3.

The impact of intraporous resistances combined with that of NH_3 inhibition is also visible from the values of the effectiveness

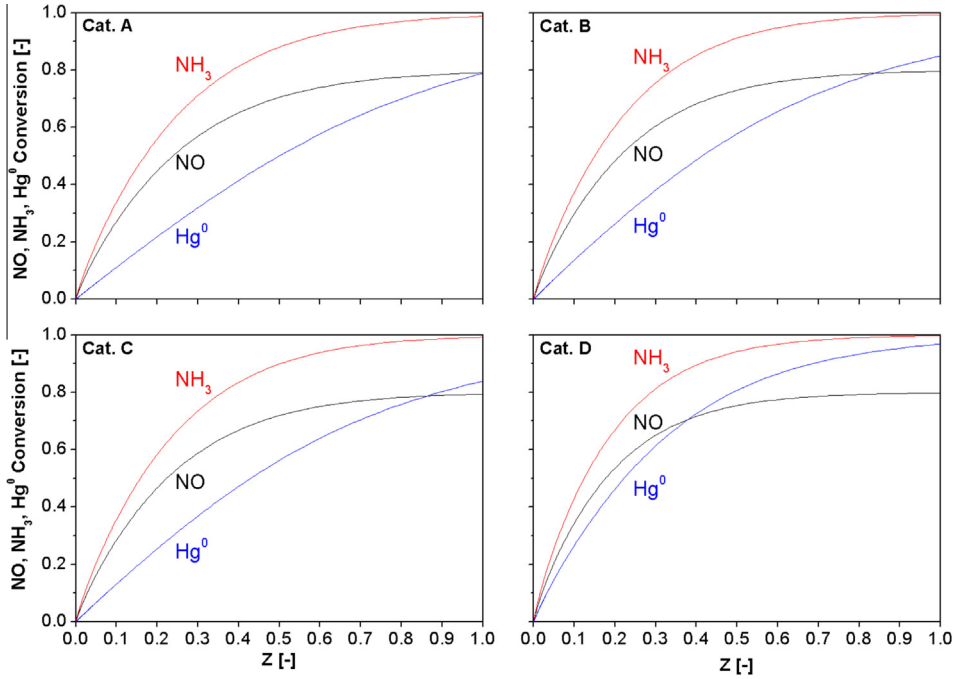

Fig. 10. NO, NH_3 and Hg^0 calculated conversion over the normalized reactor axial coordinate for Catalysts A, B, C and D. Operating conditions: AV = 7 Nm/h; T = 300 °C; $\alpha = 0.8$; $C^0_{NO} = 300$ ppm; $C^0_{Hg} = 20$ μg/Nm^3.

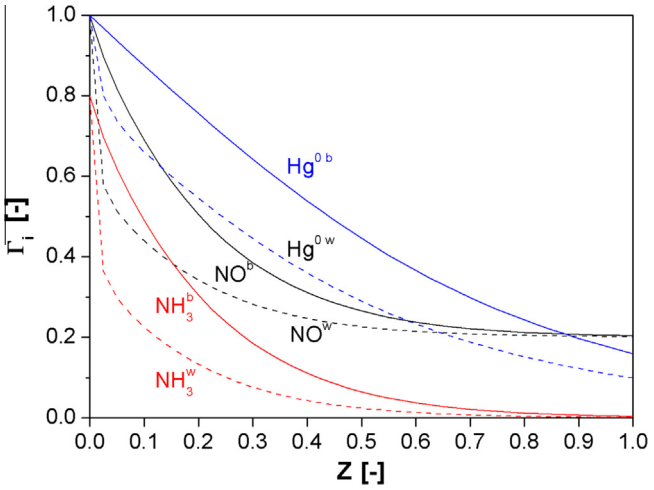

Fig. 11. Calculated NO, NH_3 and Hg^0 concentration profiles in the bulk (solid lines) and at the wall (dotted lines) concentration along the normalized axial coordinate for Catalysts B. Operating conditions: AV = 7 Nm/h; T = 300 °C; $\alpha = 0.8$; $C^0_{NO} = 300$ ppm; $C^0_{Hg} = 20$ μg/Nm^3.

factors of the two processes, which are also calculated in Fig. 12. At the reactor entrance ($z/L = 0.025$) the effectiveness factor of Hg^0 oxidation is twice as that of the $DeNO_X$ reaction; here NH_3 inhibition is mostly important and elemental mercury can penetrate deeper than NH_3 inside the catalyst wall. At increasing z/L, while NH_3 inhibition becomes less and less pronounced, the effectiveness factor of Hg^0 oxidation tends to become closer to the effectiveness factor of the $DeNO_X$ process.

Fig. 13 shows the calculated internal profiles of Hg^0 oxidation rate along the reactor for AV = 7 Nm/h (operation of the full scale reactor with three catalyst layers); it is shown that the rate of Hg^0 oxidation grows along the first half of the reactor due to the progressive consumption of NH_3, while it decreases again along the rest of the bed because of the decreasing concentration of Hg^0.

In summary, an overall analysis of the reactor performance under reference operating conditions and reference catalyst reactivity, as herein examined, suggests that:

(a) external mass transfer has a very important limiting effect on the kinetics of the $DeNO_X$ reaction, so that NH_3 concentration at the gas–solid interface is much lower than the gas-phase concentration; additionally, intraporous resistances are such that the $DeNO_X$ reaction occurs within a very thin superficial layer. As a consequence, under substoichiometric NH_3/NO values the amount of NH_3 within the monolith wall is small and reduces rapidly along the axial coordinate of the reactor with the progress of NO_X conversion.

(b) in spite of the relatively slow molecular diffusion of Hg^0, external mass transfer limitations have a less dramatic impact on Hg^0 conversion than on NH_3 and NO_X conversion. The oxidation of mercury is in fact a slower catalytic process; this is affected by intraporous limitations, so that also this process proceeds on a superficial layer of catalyst, wherein NH_3 also penetrates. From the simulations of the pilot scale reactor at AV = 21 and 7 Nm/h, we observe that in the first layer of a three-layers SCR full scale reactor, the rate of Hg^0 oxidation is slowed down because of NH_3 inhibition. The inhibiting effect becomes instead negligible in the ending portion of the full scale reactor, because of the substantial depletion of NH_3 within the wall.

7. A parametric analysis of the reactor performance at varying operating conditions and catalyst reactivity

The analysis of the processes and in particular the impact of NH_3 inhibition on Hg^0 oxidation were examined in a wider field, considering in particular the effects of NH_3/NO feed ratio and of the catalyst intrinsic reactivity.

In the previous paragraph we have seen that under a substoichiometric feed ratio, NH_3 concentration is extremely small within

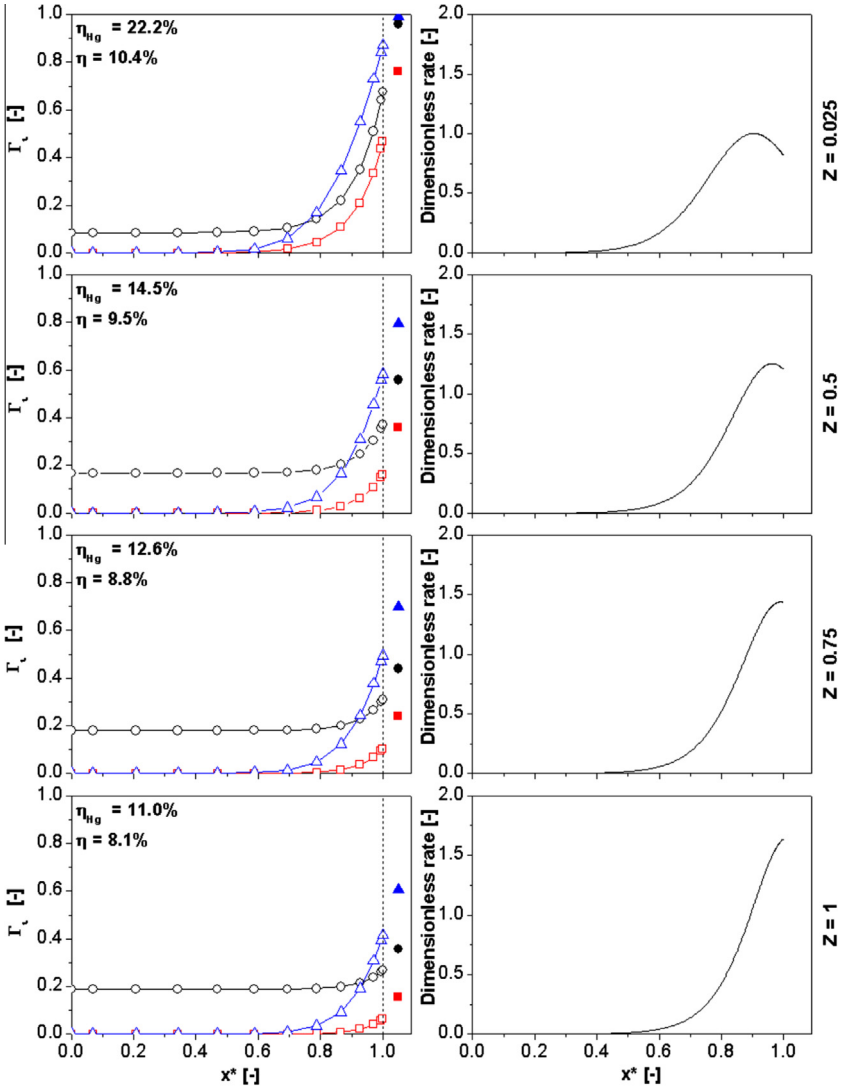

Fig. 12. Calculated NO (black empty circles), NH_3 (red empty squares) and Hg^0 (blue empty triangles) concentration profiles and (in right had panels) Hg^0 oxidation dimensionless rate along the normalized intraporous coordinate for different axial coordinate, Catalyst B. Full symbols: calculated bulk concentration. Operating conditions: AV = 21 Nm/h; T = 300 °C; α = 0.8; C^0_{NO} = 300 ppm; C^0_{Hg} = 20 μg/Nm^3. Hg^0 oxidation dimensionless rate = $\frac{s \cdot h}{D_{Hg}}\left(\frac{k_{Hg}\Gamma^{wall}_{Hg}}{1+K_{NH_3Hg}\Gamma^{wall}_{NH_3}}\right)$. (For interpretation of the references to colour in this figure legend, the reader is referred to the web version of this article.)

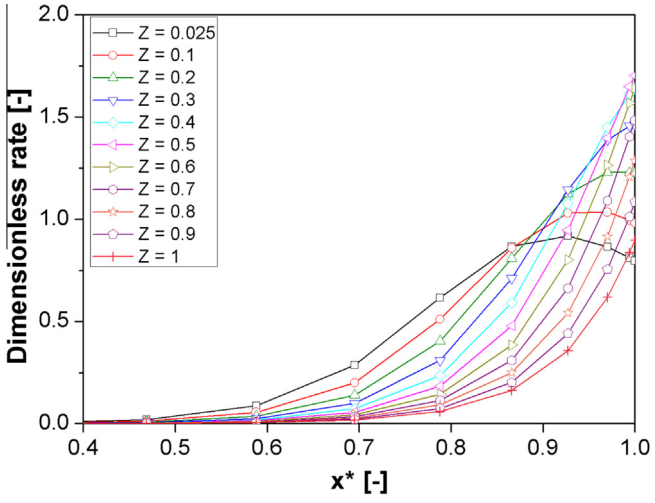

Fig. 13. Calculated Hg^0 oxidation dimensionless rate along the normalized intraporous coordinate for different axial coordinates, Catalyst B. Operating conditions: AV = 7 Nm/h; T = 300 °C; α = 0.8; C^0_{NO} = 300 ppm; C^0_{Hg} = 20 μg/Nm^3.

the wall, except for the inlet reactor zone, and this limits the integral effect of NH_3 inhibition on Hg^0 oxidation at sufficiently low AV values. However, at NH_3/NO feed ratios equal to one or higher, NH_3 diffuses within the entire catalyst wall; in this case, the inhibition on Hg^0 oxidation is present throughout the entire reactor volume.

Fig. 14 provides the overall view of the impact of α on the calculated Hg^0 conversion at various values of AV. It is shown that at the lowest AV values (7 and 10 Nm/h), the integral effect of NH_3 inhibition is little for NH_3/NO < 1 (Hg^0 conversion is in fact almost constant), and a net decrease of Hg^0 conversion occurs only at $\alpha \geqslant 1$.

At high values of the area velocity (21 and 30 Nm/h), the sensitivity of mercury oxidation on NH_3 concentration is more important. A moderate slope of Hg^0 conversion is present also at $\alpha < 1$; this is the result of the inhibiting effect that NH_3 ammonia exerts on Hg^0 oxidation in the entry portion of the reactor. Besides, at $\alpha \geqslant 1$, the drop of Hg^0 conversion becomes even more pronounced.

We have verified the sensitivity of the integral effect of NH_3/NO versus representative kinetic parameters. Fig. 15 examines the sensitivity of the reactor performance on changes of the ammonia

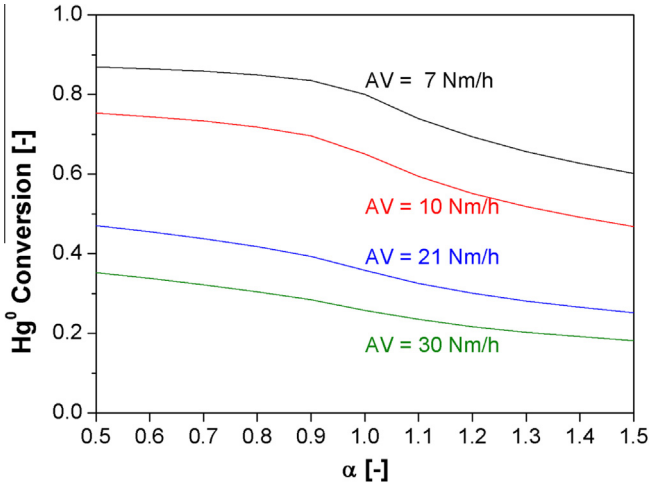

Fig. 14. Parametric analysis: calculated effect of AV on Hg^0 conversion at varying α for Catalyst B. Operating conditions: $T = 300$ °C; $C^0_{NO} = 300$ ppm; $C^0_{Hg} = 20$ μg/Nm^3.

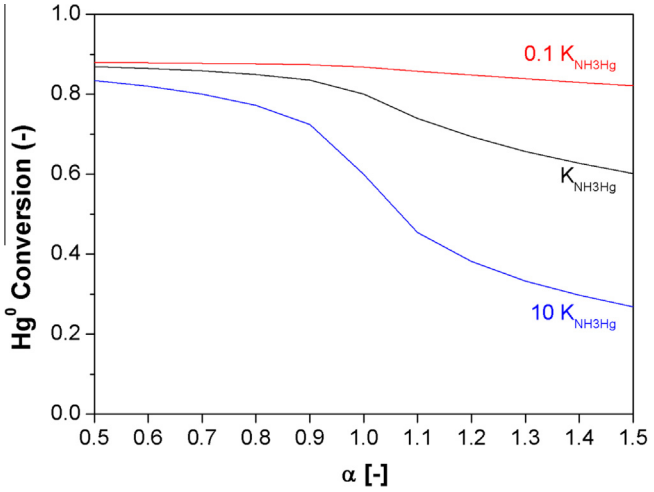

Fig. 15. Parametric analysis: calculated effect of K_{NH_3}Hg on Hg^0 conversion at varying α, Catalyst B. Operating conditions: AV = 7 Nm/h; $T = 300$ °C; C^0_{NO} = 300 ppm; $C^0_{Hg} = 20$ μg/Nm^3.

inhibition parameter $K_{NH_3\text{-}Hg}$ at fixed intrinsic rate constant, k_{Hg}. This parameter is crucial in determining the entity of NH_3 inhibition and the extent of the Hg^0 conversion drop at increasing alfa values. It has a tremendous effect both at low and at high AV values. This suggests that the tailoring of the catalyst (e.g. the acidity of the active element and of the support) may represent a key to weaken NH_3 adsorption and its inhibiting effect on Hg^0 oxidation. Also, this consideration opens the opportunity of designing activity profiles in the SCR reactor, exploiting for instance the intrinsic modularity (the layers of catalysts) of the reactor.

Fig. 16 shows then the calculated effect of k_{DeNO_X} at constant k_{Hg}. A decrease of the intrinsic $DeNO_X$ reactivity (which could result for instance from the catalyst ageing) has an impact on the sensitivity of Hg^0 conversions versus α. While for a catalyst with reference $DeNO_X$ activity as in the case of catalyst B, the Hg^0 conversion curve is affected by NH_3 inhibition at $\alpha = 1$, a tenfold reduction of the $DeNO_X$ reactivity produces a progressive decrease of Hg^0 conversion at increasing alfa. This is due to the fact at lower $DeNO_X$ reactivity, more NH_3 is present in the reactor not only because of the reduced rate of consumption, but also because of the reduced impact of external and intraporous mass transfer limitations. In fact, higher concentrations of NH_3 are calculated at the wall and

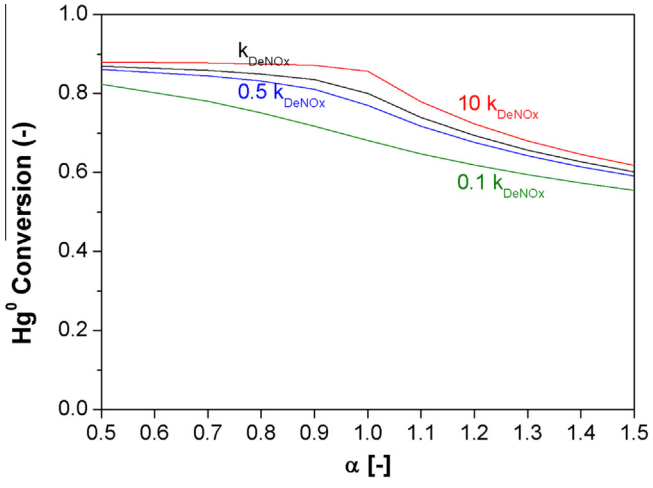

Fig. 16. Parametric analysis: calculated effect of k_{DeNO_X} on calculated Hg^0 conversion at varying α for Catalyst B. Operating conditions: AV = 7 Nm/h; $T = 300$ °C; $\alpha = 0.8$; $C^0_{NO} = 300$ ppm; $C^0_{Hg} = 20$ μg/Nm^3.

within the catalyst wall, so that the effective volume of catalyst wherein Hg^0 oxidation is inhibited by NH_3 tends to increase. Conversely, a tenfold increase of the $DeNO_X$ intrinsic reactivity decreases the sensitivity of Hg^0 oxidation on α since NH_3 concentration at the gas–solid interface and inside the wall decrease significantly.

As a final comment, the present analysis shows that the extent of NH_3 inhibition on Hg^0 conversion depends in general terms on the specific reactivity properties of the catalysts, however the operation at $\alpha < 1$ and at sufficiently low AV represent conservative conditions that minimize the integral effect of ammonia inhibition on Hg^0 conversion. The tailoring of the catalyst properties becomes more stringent for operations of the SCR reactor at NH_3/NO values close to 1, a condition which increases the amount of ammonia inside the reactor.

This work differs from previous modeling studies and provides a complete kinetic characterization of the commercial catalysts with estimates of all the relevant parameters; it represents a rigorous chemical engineering tool useful for the tailoring of the catalyst (e.g. geometry of the monolith, morphology of the catalysts, activity profiles) and of the reactor configuration (e.g. design of differentiated catalyst layers).

Future developments of this work will try to improve the description of the chemistry of the several species involved, including the nature of the active sites and the role of HCl.

Appendix A. Supplementary data

- Supplementary data associated with this article can be found, in the online version.

References

[1] Y. Gao, Z. Zhang, J. Wu, L. Duan, A. Umar, L. Sun, Z. Guo, Q. Wang, A critical review on the heterogeneous catalytic oxidation of elemental mercury in flue gases, Environ. Sci. Technol. 47 (2013) 10813–10823.
[2] B.M. Reddy, N. Durgasri, T.V. Kumar, S.K. Bhargava, Abatement of gas-phase mercury-recent developments, Catal. Rev. Sci. Eng. 54 (2012) 344–398.
[3] EPA, Mercury and air toxics standards (MATS), in, 2011.
[4] Y.E. Yudovich, M.P. Ketris, Mercury in coal: a review Part 2. Coal use and environmental problems, Int. J. Coal Geol. 62 (2005) 135–165.
[5] J.H. Pavlish, E.A. Sondreal, M.D. Mann, E.S. Olson, K.C. Galbreath, D.L. Laudal, S.A. Benson, Status review of mercury control options for coal-fired power plants, Fuel Process. Technol. 82 (2003) 89–165.
[6] T.D. Brown, D.N. Smith, R.A. Hargis Jr, W.J. O'Dowd, Mercury measurement and its control: What we know, have learned, and need to further investigate, J. Air Waste Manag. Assoc. 49 (1999) 628–640.

[7] Y. Tan, R. Mortazavi, B. Dureau, M.A. Douglas, An investigation of mercury distribution and speciation during coal combustion, Fuel 83 (2004) 2229–2236.
[8] S.J. Lee, Y.C. Seo, H.N. Jang, K.S. Park, J.I. Baek, H.S. An, K.C. Song, Speciation and mass distribution of mercury in a bituminous coal-fired power plant, Atmos. Environ. 40 (2006) 2215–2224.
[9] L.V. Heebink, D.J. Hassett, Mercury release from FGD, Fuel 84 (2005) 1372–1377.
[10] A.A. Presto, E.J. Granite, Noble metal catalysts for mercury oxidation in utility flue gas, Platin. Met. Rev. 52 (2008) 144–154.
[11] J.A. Hrdlicka, W.S. Seames, M.D. Mann, D.S. Muggli, C.A. Horabik, Mercury oxidation in flue gas using gold and palladium catalysts on fabric filters, Environ. Sci. Technol. 42 (2008) 6677–6682.
[12] Y. Zhao, M.D. Mann, J.H. Pavlish, B.A.F. Mibeck, G.E. Dunham, E.S. Olson, Application of gold catalyst for mercury oxidation by chlorine, Environ. Sci. Technol. 40 (2006) 1603–1608.
[13] Z. Mei, Z. Shen, Y. Zhang, F. Xiang, J. Chen, W. Wang, The effect of N-doping and halide-doping on the activity of $CuCoO_4$ for the oxidation of elemental mercury, Appl. Catal. B 78 (2008) 112–119.
[14] A. Yamaguchi, H. Akiho, S. Ito, Mercury oxidation by copper oxides in combustion flue gases, Powder Technol. 180 (2008) 222–226.
[15] P. Wang, S. Su, J. Xiang, F. Cao, L. Sun, S. Hu, S. Lei, Catalytic oxidation of Hg^0 by $CuO–MnO_2–Fe_2O_3/\gamma\text{-}Al_2O_3$ catalyst, Chem. Eng. J. 225 (2013) 68–75.
[16] X. Li, Z. Liu, J. Kim, J.Y. Lee, Heterogeneous catalytic reaction of elemental mercury vapor over cupric chloride for mercury emissions control, Appl. Catal. B 132–133 (2013) 401–407.
[17] H. Kamata, S.I. Ueno, T. Naito, A. Yukimura, Mercury oxidation over the $V_2O_5(WO_3)/TiO_2$ commercial SCR catalyst, Ind. Eng. Chem. Res. 47 (2008) 8136–8141.
[18] H. Kamata, S.I. Ueno, T. Naito, A. Yamaguchi, S. Ito, Mercury oxidation by hydrochloric acid over a VO_x/TiO_2 catalyst, Catal. Commun. 9 (2008) 2441–2444.
[19] S. Straube, T. Hahn, H. Koeser, Adsorption and oxidation of mercury in tail-end SCR-$DeNO_X$ plants-Bench scale investigations and speciation experiments, Appl. Catal. B 79 (2008) 286–295.
[20] H.J. Hong, S.W. Ham, M.H. Kim, S.M. Lee, J.B. Lee, Characteristics of commercial selective catalytic reduction catalyst for the oxidation of gaseous elemental mercury with respect to reaction conditions, Korean J. Chem. Eng. 27 (2010) 1117–1122.
[21] H. Sheng, Z. Jinsong, Z. Yanqun, L. Zhongyang, N. Mingjiang, C. Kefa, Mercury oxidation over a vanadia-based selective catalytic reduction catalyst, Energy Fuels 23 (2009) 253–259.
[22] S. Eswaran, H.G. Stenger, Understanding mercury conversion in selective catalytic reduction (SCR) catalysts, Energy Fuels 19 (2005) 2328–2334.
[23] Y. Zhuang, J. Laumb, R. Liggett, M. Holmes, J. Pavlish, Impacts of acid gases on mercury oxidation across SCR catalyst, Fuel Process. Technol. 88 (2007) 929–934.
[24] S. Eswaran, H.G. Stenger, Effect of halogens on mercury conversion in SCR catalysts, Fuel Process. Technol. 89 (2008) 1153–1159.
[25] R. Stolle, H. Koeser, H. Gutberlet, Oxidation and reduction of mercury by SCR $DeNO_X$ catalysts under flue gas conditions in coal fired power plants, Appl. Catal. B 144 (2013) 486–497.
[26] S. Niksa, N. Fujiwara, A predictive mechanism for mercury oxidation on selective catalytic reduction catalysts under coal-derived flue gas, J. Air Waste Manag. Assoc. 55 (2005) 1866–1875.
[27] C.L. Senior, Oxidation of mercury across selective catalytic reduction catalysts in coal-fired power plants, J. Air Waste Manag. Assoc. 56 (2006) 23–31.
[28] W. Gao, Q. Liu, C.Y. Wu, H. Li, Y. Li, J. Yang, G. Wu, Kinetics of mercury oxidation in the presence of hydrochloric acid and oxygen over a commercial SCR catalyst, Chem. Eng. J. 220 (2013) 53–60.
[29] H. Kamata, S.I. Ueno, N. Sato, T. Naito, Mercury oxidation by hydrochloric acid over TiO_2 supported metal oxide catalysts in coal combustion flue gas, Fuel Process. Technol. 90 (2009) 947–951.
[30] H. Li, C.Y. Wu, Y. Li, J. Zhang, Superior activity of $MnO_x–CeO_2/TiO_2$ catalyst for catalytic oxidation of elemental mercury at low flue gas temperatures, Appl. Catal. B 111–112 (2012) 381–388.
[31] J.A.D. Madsen K., Thogersen J.R., Frandsen F., A mechanistic study on the inhibition reaction on the mercury oxidation over SCR catalysts, in: Air Quality VII Conference, Arlington, 2011.
[32] J.A.D. Madsen K., Thogersen J.R., Frandsen F., Mercury Oxidation over SCR Catalysts for NO_X control, in: ICC 2012, Munich, 2012.
[33] F. Frandsen, K. Dam-Johansen, P. Rasmussen, Trace elements from combustion and gasification of coal – an equilibrium approach, Prog. Energy Combust. Sci. 20 (1994) 115–138.
[34] K.C. Galbreath, C.J. Zygarlicke, Mercury speciation in coal combustion and gasification flue gases, Environ. Sci. Technol. 30 (1996) 2421–2426.
[35] T. Nishitani, I. Fukunaga, H. Itoh, T. Nomura, The relationship between HCL and mercury speciation in flue gas from municipal solid waste incinerators, Chemosphere 39 (1999) 1–9.
[36] H. Kamata, A. Yukimura, Catalyst aging in a coal combustion flue gas for mercury oxidation, Fuel Process. Technol. 104 (2012) 295–299.
[37] H. Li, Y. Li, C.Y. Wu, J. Zhang, Oxidation and capture of elemental mercury over $SiO_2–TiO_2–V_2O_5$ catalysts in simulated low-rank coal combustion flue gas, Chem. Eng. J. 169 (2011) 186–193.
[38] J. Liu, M. He, C. Zheng, M. Chang, Density functional theory study of mercury adsorption on V_2O_5 (001) surface with implications for oxidation, Proc. Combust. Inst. 33 (2011) 2771–2777.
[39] A.S. Negreira, J. Wilcox, Role of WO_3 in the Hg oxidation across the $V_2O_5–WO_3–TiO_2$ SCR catalyst: a DFT study, J. Phys. Chem. C 117 (2013) 24397–24406.
[40] A. Suarez Negreira, J. Wilcox, DFT study of Hg oxidation across vanadia–titania SCR catalyst under flue gas conditions, J. Phys. Chem. C 117 (2013) 1761–1772.
[41] S. Niksa, A.F. Sibley, Predicting the multipollutant performance of utility SCR systems, Ind. Eng. Chem. Res. 49 (2010) 6332–6341.
[42] C. Orsenigo, A. Beretta, P. Forzatti, J. Svachula, E. Tronconi, F. Bregani, A. Baldacci, Theoretical and experimental study of the interaction between NO_X reduction and SO_2 oxidation over $DeNO_X$-SCR catalysts, Catal. Today 27 (1996) 15–21.
[43] E. Tronconi, P. Forzatti, J.P. Gomez Martin, S. Mallogi, Selective catalytic removal of NO_X: a mathematical model for design of catalyst and reactor, Chem. Eng. Sci. 47 (1992) 2401–2406.
[44] E. Tronconi, A. Beretta, A.S. Elmi, P. Forzatti, S. Malloggi, A. Baldacci, A complete model of scr monolith reactors for the analysis of interacting NO_X reduction and SO_2 oxidation reactions, Chem. Eng. Sci. 49 (1994) 4277–4287.
[45] B. Heidel, S. Farr, K. Brechtel, G. Scheffknecht, H. Thorwarth, Influencing factors on the emission of mercury from wet flue gas desulphurisation slurries, VGB PowerTech 92 (2012) 64–70.
[46] A. Bianchi, V. Borghini, M. Cioni, Continuous mercury species monitoring in exhaust gas, Combustion and the Environment, in: 24th Event of the Italian Section of the Combustion Institute, 17–19 September 2001.
[47] A. Bianchi, V. Borghini, A. Paolicchi, L. Casali, C. La Marca, M. Cioni, Testing a novel instrument for Hg^0 and Hg^{2+} monitoring in the flue gas, in: Joint Meeting of the Scadinavian Nordic and Italian Sectors of Combustion Institute, 18–21 September 2003.
[48] E. Tronconi, P. Forzatti, Adequacy of lumped parameter models for SCR reactors with monolith structure, AIChE J. 38 (1992) 201–210.
[49] NIST Chemistry WebBook, 2013, http://webbook.nist.gov/chemistry/.
[50] A. Beretta, C. Orsenigo, N. Ferlazzo, E. Tronconi, P. Forzatti, F. Berti, Analysis of the performance of plate-type monolithic catalysts for selective catalytic reduction $DeNO_X$ applications, Ind. Eng. Chem. Res. 37 (1998) 2623–2633.
[51] E.N. Fuller, P.D. Schettler, J.C. Giddings, New method for prediction of binary gas-phase diffusion coefficients, Ind. Eng. Chem. Res. 58 (1966) 18–27.
[52] W.J. Massman, Molecular diffusivities of Hg vapor in air, O_2 and N_2 near STP and the kinematic viscosity and thermal diffusivity of air near STP, Atmos. Environ. 33 (1999) 453–457.
[53] N. Wakao, J.M. Smith, Diffusion in catalyst pellets, Chem. Eng. Sci. 17 (1962) 825–834.
[54] P. Forzatti, Present status and perspectives in de-NO_X SCR catalysis, Appl. Catal. A 222 (2001) 221–236.
[55] P. Forzatti, L. Lietti, Recent advances in de-NOxing catalysis for stationary applications, Heterogen. Chem. Rev. 3 (1996) 33–51.